# Saturation of a toroidal Alfvén eigenmode due to enhanced damping of nonlinear sidebands

**Y. Todo[1,2], H.L. Berk[3] and B.N. Breizman[3]**

[1] National Institute for Fusion Science, Toki, Japan
[2] Department of Fusion Science, The Graduate University for Advanced Studies
(SOKENDAI), Toki, Japan
[3] Institute for Fusion Studies, University of Texas at Austin, Austin, TX, USA

E-mail: todo@nifs.ac.jp

## Abstract

This paper examines nonlinear magneto-hydrodynamic effects on the energetic particle driven toroidal Alfvén eigenmode (TAE) for lower dissipation coefficients and with higher numerical resolution than in the previous simulations (Todo *et al* 2010 *Nucl. Fusion* **50** 084016). The investigation is focused on a TAE mode with toroidal mode number $n = 4$. It is demonstrated that the mechanism of mode saturation involves generation of zonal ($n = 0$) and higher-$n$ ($n \geqslant 8$) sidebands, and that the sidebands effectively increase the mode damping rate via continuum damping. The $n = 0$ sideband includes the zonal flow peaks at the TAE gap locations. It is also found that the $n = 0$ poloidal flow represents a balance between the nonlinear driving force from the $n = 4$ components and the equilibrium plasma response to the $n = 0$ fluctuations. The spatial profile of the $n = 8$ sideband peaks at the $n = 8$ Alfvén continuum, indicating enhanced dissipation due to continuum damping.

## 1. Introduction

This paper extends our recent work [1] in which we investigated the effects of magneto-hydrodynamic (MHD) nonlinearity on Alfvén eigenmode instability using hybrid simulations of MHD fluid interacting with energetic particles. To clarify the role of the MHD nonlinearity, the nonlinear MHD results were compared with simulations in which only linear MHD equations were solved together with a nonlinear response of the energetic particles. At a low saturation level of the excited mode ($\delta B/B \leqslant 10^{-3}$), no significant difference was found between the results of the linear MHD and the nonlinear MHD simulations. On the other hand, when the mode saturation level was $\delta B/B \sim 10^{-2}$ in the linear MHD simulation, the nonlinear MHD simulation showed only half of that level. We found that the nonlinearly generated $n = 0$ and higher-$n$ sidebands provide increased dissipation that appears to be responsible for the reduced saturation level. The total dissipation increases despite the fact that the dissipation from the $n = 4$ component alone decreases slightly before saturation. This mechanism is different from the one discussed in [2, 3] where the nonlinearity would increase the damping rate of the dominant $n = 4$ mode directly.

The need to examine nonlinear MHD effects is evident from previous simulations [4] of the toroidal Alfvén eigenmode

(TAE) bursts in a Tokamak Fusion Test Reactor (TFTR) experiment [5]. Many of the experimental characteristics, such as (a) the synchronization of multiple TAEs, (b) the modulation depth of the drop in the stored beam energy, (c) the stored beam energy, were reproduced in those simulations. However, the saturation amplitude of the TAE modes was $\delta B/B \sim 2 \times 10^{-2}$ which is considerably higher than the value $\delta B/B \sim 10^{-3}$ inferred from the experimental plasma displacement measurements at the plasma edge [6]. In the simulation of [4], the only nonlinearity retained was the nonlinearity in the energetic particle orbits, while the nonlinear MHD effects were neglected. This suggested that the MHD nonlinearity may need to be included in the simulations.

Recently, we have extended the MEGA code [7–9], which is a hybrid simulation code for an MHD fluid interacting with energetic particles, by implementing the energetic particle source, collisions and losses. We used two versions of the MEGA code, with either linear or nonlinear MHD equations employed, to study the nonlinear MHD effects on TAE bursts [10]. It was demonstrated for physical parameters close to the TFTR experiment that the nonlinear MHD effects reduce the saturation amplitude to a level $\delta B_{m/n}/B \sim 5 \times 10^{-3}$ for the dominant harmonic of the radial magnetic fluctuation. The TAE bursts take place with a time interval close to the experiment. The stored beam energy drop associated with

each burst has a modulation depth of roughly 10%, which is also close to the experimental value of 7%.

In this work, we study the nonlinear MHD effects on the TAE instability with toroidal mode number $n = 4$ for lower dissipation coefficients and with higher numerical resolution than in the previous work [1]. This clarifies the spatial profiles of the nonlinear sidebands and the mechanism of sideband formation. We demonstrate that the saturation amplitude of the TAE mode reduces due to generation of zonal ($n = 0$) and higher-$n$ ($n \geqslant 8$) sidebands. This reduction results from dissipation associated with the sidebands. The $n = 0$ sideband that includes the zonal flow peaks at the TAE gap locations. The $n = 0$ poloidal flow is governed by the nonlinear coupling of the $n = 4$ components and the equilibrium plasma response to the $n = 0$ fluctuations. The spatial profile of the $n = 8$ sideband peaks at the $n = 8$ Alfvén continuum, which apparently enhances dissipation via continuum damping [11, 12].

## 2. Simulation model

Several hybrid simulation models have been constructed [13–17] to study the evolution of Alfvén eigenmodes destabilized by energetic particles. In the MEGA code, the bulk plasma is described by the nonlinear MHD equations and the energetic ions are simulated with the $\delta f$ particle method. The MHD equations with the energetic-ion effects are given by

$$\frac{\partial \rho}{\partial t} = -\nabla \cdot (\rho \boldsymbol{v}) + \nu_{\mathrm{n}} \Delta (\rho - \rho_{\mathrm{eq}}), \tag{1}$$

$$\rho \frac{\partial}{\partial t} \boldsymbol{v} = -\rho \vec{\omega} \times \boldsymbol{v} - \rho \nabla \left( \frac{v^2}{2} \right) - \nabla p + (\boldsymbol{j} - \boldsymbol{j}_h') \times \boldsymbol{B}$$
$$+ \frac{4}{3} \nabla (\nu \rho \nabla \cdot \boldsymbol{v}) - \nabla \times (\nu \rho \vec{\omega}), \tag{2}$$

$$\frac{\partial \boldsymbol{B}}{\partial t} = -\nabla \times \boldsymbol{E}, \tag{3}$$

$$\frac{\partial p}{\partial t} = -\nabla \cdot (p \boldsymbol{v}) - (\gamma - 1) p \nabla \cdot \boldsymbol{v} + (\gamma - 1)$$
$$\times \left[ \nu \rho \omega^2 + \frac{4}{3} \nu \rho (\nabla \cdot \boldsymbol{v})^2 + \eta \boldsymbol{j} \cdot (\boldsymbol{j} - \boldsymbol{j}_{\mathrm{eq}}) \right]$$
$$+ \nu_{\mathrm{n}} \Delta (p - p_{\mathrm{eq}}), \tag{4}$$

$$\boldsymbol{E} = -\boldsymbol{v} \times \boldsymbol{B} + \eta (\boldsymbol{j} - \boldsymbol{j}_{\mathrm{eq}}), \tag{5}$$

$$\boldsymbol{j} = \frac{1}{\mu_0} \nabla \times \boldsymbol{B}, \tag{6}$$

$$\vec{\omega} = \nabla \times \boldsymbol{v}, \tag{7}$$

where $\mu_0$ is the vacuum magnetic permeability, $\gamma = 5/3$ is the adiabatic constant, $\nu$ and $\nu_{\mathrm{n}}$ are artificial viscosity and diffusion coefficients chosen to maintain numerical stability and all the other quantities are conventional. The subscript 'eq' represents the equilibrium variables. The energetic-ion contribution is included in the MHD momentum equation (equation (2)) as the energetic-ion current

$$\boldsymbol{j}_h'(\boldsymbol{x}) = \sum_{i=1}^{N} w_i Z_h e (\boldsymbol{v}_{\parallel i}^* + \boldsymbol{v}_{Bi}) S(\boldsymbol{x} - \boldsymbol{x}_i)$$
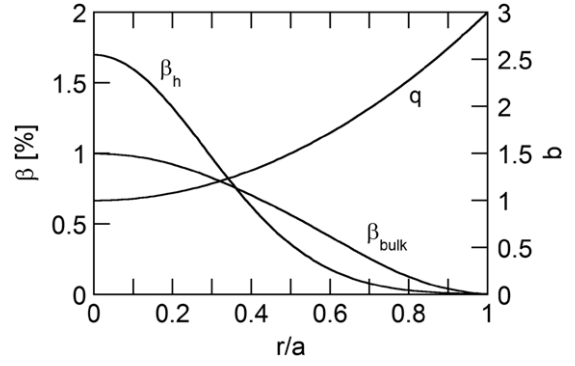$$- \nabla \times \left[ \boldsymbol{b} \sum_{i=1}^{N} w_i \mu_i S(\boldsymbol{x} - \boldsymbol{x}_i) \right] \tag{8}$$



**Figure 1.** Spatial profiles of energetic-ion beta, bulk plasma beta and safety factor.

where $w_i$, $\boldsymbol{v}_{\parallel i}^*$, $\boldsymbol{v}_{Bi}$, $S(\boldsymbol{x} - \boldsymbol{x}_i)$ and $\mu_i$ are weight, sum of parallel velocity and magnetic curvature drift, magnetic gradient drift, shape factor and magnetic moment of $i$th particle, respectively. $Z_h e$ is the energetic-ion charge. The second term of equation (8) represents the magnetization current. The $\boldsymbol{E} \times \boldsymbol{B}$ contribution to $\boldsymbol{j}_h'$ is cancelled by the electrons, due to quasi-neutrality [7]. This model is accurate as long as the energetic-ion density is much less than the bulk plasma density. The MHD equations are solved using a fourth order (in both space and time) finite difference scheme. The drift-kinetic description [18] is employed for the energetic ions. The computational particles are initially loaded uniformly in the phase space.

In order to identify nonlinear MHD effects, we use linear MHD calculations for comparison. The reduced equations for the linear MHD model are

$$\frac{\partial \rho}{\partial t} = -\nabla \cdot (\rho_{\mathrm{eq}} \boldsymbol{v}) + \nu_{\mathrm{n}} \Delta (\rho - \rho_{\mathrm{eq}}), \tag{9}$$

$$\rho_{\mathrm{eq}} \frac{\partial}{\partial t} \boldsymbol{v} = -\nabla p + (\boldsymbol{j}_{\mathrm{eq}} - \boldsymbol{j}_{h_{\mathrm{eq}}}') \times \delta \boldsymbol{B} + (\delta \boldsymbol{j} - \delta \boldsymbol{j}_h') \times \boldsymbol{B}_{\mathrm{eq}}$$
$$+ \frac{4}{3} \nabla (\nu \rho_{\mathrm{eq}} \nabla \cdot \boldsymbol{v}) - \nabla \times (\nu \rho_{\mathrm{eq}} \vec{\omega}), \tag{10}$$

$$\frac{\partial \boldsymbol{B}}{\partial t} = -\nabla \times \boldsymbol{E}, \tag{11}$$

$$\frac{\partial p}{\partial t} = -\nabla \cdot (p_{\mathrm{eq}} \boldsymbol{v}) - (\gamma - 1) p_{\mathrm{eq}} \nabla \cdot \boldsymbol{v} + (\gamma - 1) \eta \delta \boldsymbol{j} \cdot \boldsymbol{j}_{\mathrm{eq}}$$
$$+ \nu_{\mathrm{n}} \Delta (p - p_{\mathrm{eq}}), \tag{12}$$

$$\boldsymbol{E} = -\boldsymbol{v} \times \boldsymbol{B}_{\mathrm{eq}} + \eta \delta \boldsymbol{j}. \tag{13}$$

Here the variables with $\delta$ such as $\delta \boldsymbol{B}$ represent the fluctuations, for example, $\delta \boldsymbol{B} = \boldsymbol{B} - \boldsymbol{B}_{\mathrm{eq}}$.

A tokamak plasma with aspect ratio of $R_0/a = 3.2$ was investigated where $R_0$ and $a$ are the major radius of the geometrical centre of the simulation domain and the plasma minor radius, respectively. The cylindrical coordinates $(R, \varphi, z)$ are employed. The shape of the outermost magnetic surface is circular. The spatial profiles of the energetic-ion beta, bulk plasma beta, and safety factor are shown in figure 1. The bulk plasma density is uniform. The central energetic-ion beta $\beta_{h0}$ is 1.7%. The initial distribution of the energetic ions is a slowing-down distribution with a maximum velocity $1.2 v_{\mathrm{A}}$ and the critical velocity $0.5 v_{\mathrm{A}}$, where $v_{\mathrm{A}}$ denotes the Alfvén velocity at the plasma centre. The ratio of the energetic-ion Larmor radius to the minor radius is 1/16 for the energetic-ion

velocity equal to the Alfvén velocity. We neglect the finite Larmor radius effect for the energetic ions. This will lead to an overestimate of the instability growth rate, although the effect is partly mitigated due to the finite orbit arising from the magnetic curvature and magnetic gradient drifts [19]. In our previous work, we investigated nonlinear MHD effects for different energetic-ion pressure [1]. We neglected energetic-ion pressure in the equilibrium and used the same equilibrium to focus on the nonlinear MHD effects. In this work we use the same equilibrium for the purpose of comparison with the previous work.

In what follows, we limit our consideration to the case of the $n = 4$ mode, so that only the $n = 4$ component is present in the linear MHD code. The MHD nonlinearities generate fluctuations with toroidal mode numbers that are multiples of 4 ($n = 0, 4, 8, 12, 16, \ldots$). The apparent symmetry of the $n = 4$ mode and its nonlinear sidebands allows us to restrict our simulation to a quarter of the tokamak domain with $0 \leqslant \varphi \leqslant \pi/2$, where $\varphi$ is the toroidal angle. This symmetry saves the CPU time and memory compared with a full torus simulation. The energetic-ion current $\delta j'_h$ generally contains all toroidal harmonics that are multiples of 4. This produces MHD fluctuations with toroidal mode numbers that are multiples of $n = 4$ and obscures the effects of the MHD nonlinearity. We therefore retain only the $n = 4$ component of the hot particle current, while we artificially remove the energetic-ion current density fluctuation $\delta j'_h$ if $n \neq 4$.

In the previous work we investigated two sets of dissipation coefficients, the number of grid points, and the number of computational particles [1]. In the first set, the viscosity, diffusion and resistivity coefficients in the MHD equations were chosen to be $\nu = \nu_n = \eta/\mu_0 = 10^{-6} v_A R_0$, and the number of grid points for the cylindrical coordinates $(R, \varphi, z)$ was $128 \times 64 \times 128$; the number of computational particles was $5.2 \times 10^5$. The second set had lower dissipation coefficients, $\nu = \nu_n = \eta/\mu_0 = 2.5 \times 10^{-7} v_A R_0$, and a larger number of grid points and computational particles: $256 \times 128 \times 256$ and $4.2 \times 10^6$, respectively. In this paper, we further reduce the dissipation coefficients to $\nu = \nu_n = \eta/\mu_0 = 6.1 \times 10^{-8} v_A R_0$ and we increase the number of grid points and computational particles to $512 \times 128 \times 512$ and $1.7 \times 10^7$. This fine-scale grid provides adequate spatial resolution for the nonlinearly generated sidebands.

## 3. Simulation results

### 3.1. Comparison of linear MHD and nonlinear MHD simulations

The spatial profile of the unstable $n = 4$ TAE mode at the linear phase of the instability is shown in figure 2. A magnetic flux coordinate system $(r, \varphi, \vartheta)$ is constructed for data analysis. The phase of the mode in the figure is chosen so that the cosine part of the dominant harmonic $m/n = 6/4$ is maximized at the peak location. Evolution of the radial velocity $v_r/v_A$ is presented in figure 3 for linear and nonlinear MHD simulations. Figure 3 shows the $m/n = 6/4$ component of $v_r/v_A$ measured at the TAE peak location $r = 0.44a$. The frequency and the growth rate of the TAE are $\omega = 0.309\omega_A$ and $\gamma = 4.6 \times 10^{-2}\omega_A$, respectively, with $\omega_A = v_A/R_{\text{axis}}$, where $R_{\text{axis}}$ is the major radius of the magnetic axis. Figure 3 shows
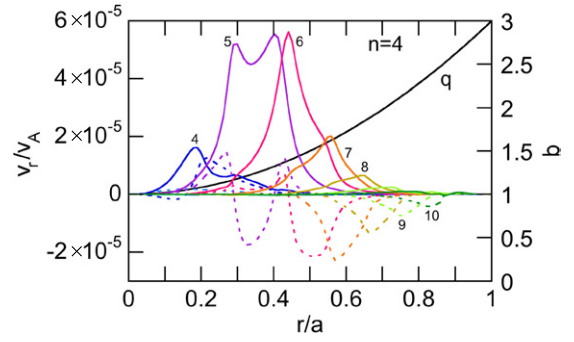


**Figure 2.** Spatial profiles of poloidal harmonics of the radial velocity in a TAE with toroidal mode number $n = 4$ for radial velocity. The figure represents a snapshot at $\omega_A t = 189$. Solid (dashed) lines show $\cos(m\vartheta + n\varphi)$ [$\sin(m\vartheta + n\varphi)$] harmonics with poloidal mode number $m$ labelled in the figure.
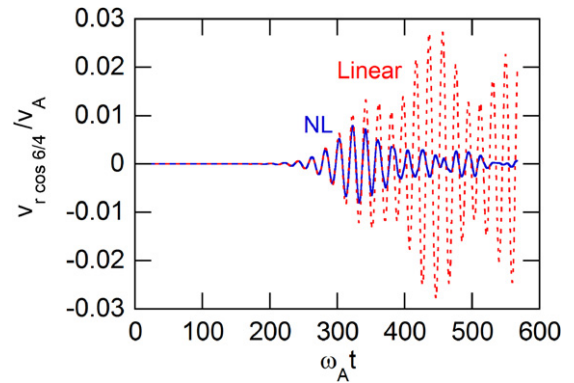


**Figure 3.** Comparison of the radial velocity evolution in the linear and nonlinear MHD runs using the cosine part of $m/n = 6/4$ harmonics at $r/a = 0.44$.

a significant reduction of the saturation level in the nonlinear MHD run. The saturation level of $v_r/v_A$ is $\sim 8 \times 10^{-3}$ for the nonlinear MHD simulation while it is $\sim 1.3 \times 10^{-2}$ at $\omega_A t \approx 340$ for the linear MHD simulation. In the linear MHD run, another unstable TAE mode (with major harmonics $m/n = 6/4$ and $7/4$) produces a second (higher) maximum in figure 3 at $\omega_A t \approx 450$.

In order to clarify the physics mechanism that reduces the TAE saturation level, we use the same approach as in the previous work [1]. We decompose the MHD fluctuations for each toroidal mode number $n \geqslant 0$. For example, the velocity fluctuation is decomposed into

$$v_n(R, \varphi, z) = v_{nc}(R, z) \cos(n\varphi) + v_{ns}(R, z) \sin(n\varphi) \quad (14)$$

$$v_{nc}(R, z) = \frac{4}{\pi} \int_0^{\pi/2} v(R, \varphi, z) \cos(n\varphi) \, d\varphi$$
$$\qquad \qquad \qquad \text{(for } n \neq 0\text{))}$$
$$v_{ns}(R, z) = \frac{4}{\pi} \int_0^{\pi/2} v(R, \varphi, z) \sin(n\varphi) \, d\varphi$$

$$(15)$$

$$v_{nc}(R, z) = \frac{2}{\pi} \int_0^{\pi/2} v(R, \varphi, z) \, d\varphi, \quad v_{ns}(R, z) = 0$$
$$\text{(for } n = 0\text{).} \qquad \qquad \qquad \qquad \qquad (16)$$

We then analyse the evolution of the MHD fluctuation energy and the energy dissipation for each toroidal mode number $n$

$$E_n \equiv \int \left( \frac{1}{2} \rho_0 v_n^2 + \frac{2\delta B_n \cdot B_{\text{eq}} + \delta B_n^2}{2\mu_0} + \frac{\delta p_n}{\gamma - 1} \right) dV, \quad (17)$$
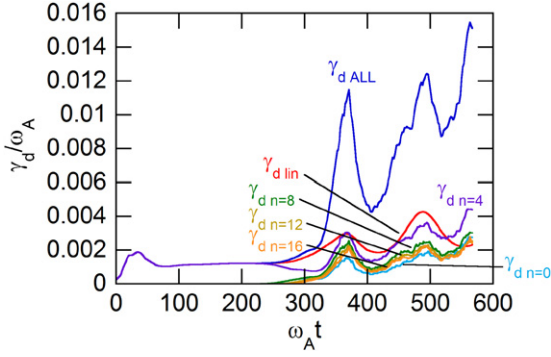
**Figure 4.** Evolution of the partial damping rates for each toroidal mode number and the total damping rate in the nonlinear MHD simulation. The curve with a label $\gamma_{d\,lin}$ shows (for comparison) the damping rate in the linear MHD simulation.

$$D_n = \int [\nu\rho_0\omega_n^2 + \frac{4}{3}\nu\rho_0(\nabla\cdot\boldsymbol{v}_n)^2 + \eta\delta\boldsymbol{j}_n\cdot\boldsymbol{j}_n]\,\mathrm{d}V. \qquad (18)$$

We found that $\sum_n D_n/2E_4$ is an effective damping rate for the cases where nonlinear coupling between the different toroidal mode numbers is essential. In figure 4 the evolution of $\gamma_{dn} = D_n/2E_4$ and $\gamma_{d\,ALL} = \sum_n D_n/2E_4$ are compared with $\gamma_{d\,lin} = D_4/2E_4$ in the linear MHD simulation. The total damping rate $\gamma_{d\,ALL}$, in the nonlinear MHD simulation, is clearly greater than the $n = 4$ TAE damping rate $\gamma_{d\,lin}$ in the linear MHD simulation. This explains why the saturation level is reduced by the MHD nonlinearity. The nonlinear coupling increases the total energy dissipation leading to a lower saturation level. The damping rate from the higher-$n$ sidebands ($n = 8, 12, 16$) is greater than that from the $n = 0$ sideband. This is different from the cases with higher dissipation coefficients shown in figures 7 and 8 in [1]. The reason why the higher-$n$ sidebands are more important for the lower dissipation coefficients is that the dissipation of the higher-$n$ sidebands arises from continuum damping. This is clarified in the next subsection. Figure 5 is a schematic diagram for energy transfer in the linear and nonlinear MHD runs. Dissipation shown in figure 5 is the resistive and viscous processes that convert magnetic and fluid kinetic energy into thermal energy. Physical damping for the TAE mode and the nonlinear sidebands included in the MHD simulations is the continuum damping that also dissipates both magnetic and fluid kinetic energy through the resistive and viscous processes.

### 3.2. Spatial profiles of nonlinear sidebands

In this subsection, we first discuss the nonlinearly driven perturbations with $n = 0$. Figure 6 shows the profiles of the $n = 0$ flow, perturbed magnetic field, density and pressure at $\omega_A t = 189$. The radial components of the flow and the magnetic field perturbations are negligibly small and are not shown in the figure. The profiles peak at the $n = 4$ TAE gap locations, $r/a = 0.25, 0.43$ and $0.55$ where the safety factor values are $q = 9/8, 11/8$ and $13/8$, respectively. The dominant harmonics are $m/n = 0/0$ and $1/0$.

In the previous work we discussed how the $n = 0$ sideband is formed [1]. When the $n = 0$ sideband is sufficiently small to neglect its feedback on the dominant ($n = 4$) mode, the
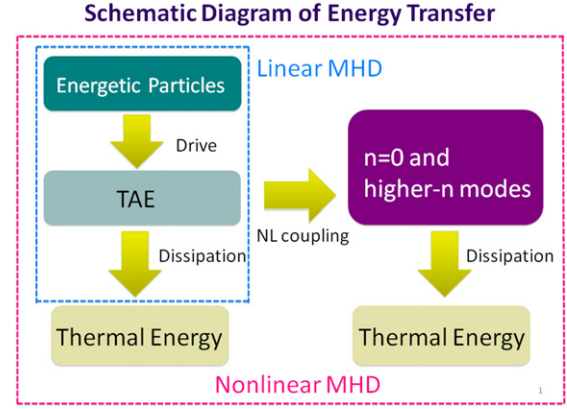


**Figure 5.** A schematic diagram of energy transfer for linear MHD and nonlinear MHD simulations.

sideband evolution can be described by the following equation:

$$\frac{\partial}{\partial t}z + M_{eq}(z) = s \qquad (19)$$

where $z$ represents the $n = 0$ perturbation $z = {}^t(\delta\rho, \delta\boldsymbol{v}, \delta\boldsymbol{B}, \delta p)$ and $M_{eq}$ is a linear MHD operator which is a function of the equilibrium variables. The source vector $s$ on the right-hand side of equation (19) is a (quadratic) contribution determined by the TAE eigenfunction. We found that $z$ grows at the rate $2\gamma_{TAE}$. Then, equation (19) is reduced to

$$2\gamma_{TAE}z + M_{eq}(z) = s. \qquad (20)$$

In this work, we analyse each term in equation (20) for the $n = 0$ poloidal flow shown in figure 6(*a*). We have three nonlinear terms for the $n = 0$ ploloidal flow in equation (2),

$$\boldsymbol{F}_1 = -\vec{\omega}_{n=4}\times\boldsymbol{v}_{n=4}, \qquad (21)$$

$$\boldsymbol{F}_2 = -\nabla\left(\frac{v_{n=4}^2}{2}\right), \qquad (22)$$

$$\boldsymbol{F}_3 = (\boldsymbol{j}_{n=4}\times\boldsymbol{B}_{n=4})/\rho_{eq}, \qquad (23)$$

where we neglected the viscous terms and divided the equation by $\rho_{eq}$. The nonlinear source for the $n = 0$ poloidal flow can be expressed as $s = \boldsymbol{F}_1 + \boldsymbol{F}_2 + \boldsymbol{F}_3$. The three nonlinear contributions to the source term for the $n = 0$ poloidal flow are shown in figure 7. These contributions are strongly localized at the $n = 4$ TAE gap which indicates that the nonlinearity involves poloidal harmonics $m$ and $m + 1$. The term $\boldsymbol{F}_2$ is negligibly small compared with $\boldsymbol{F}_1$ and $\boldsymbol{F}_3$. Next, we move the linear response term $M_{eq}(z)$ to the right-hand side, and split $-M_{eq}(z)$ into a sum of the following three terms:

$$\boldsymbol{F}_4 = -\nabla p_{n=0}, \qquad (24)$$

$$\boldsymbol{F}_5 = (\delta\boldsymbol{j}_{n=0}\times\boldsymbol{B}_{eq})/\rho_{eq}, \qquad (25)$$

$$\boldsymbol{F}_6 = (\boldsymbol{j}_{eq}\times\delta\boldsymbol{B}_{n=0})/\rho_{eq}. \qquad (26)$$

Each term for the $n = 0$ poloidal flow is shown in figure 8. Note that $\boldsymbol{F}_6$ is negligibly small compared with $\boldsymbol{F}_4$ and $\boldsymbol{F}_5$. The sum of the nonlinear source and the linear response for the $n = 0$ poloidal flow, $s - M_{eq}(z)$, is shown in figure 9(*a*). The nonlinear source $s$ and the equilibrium plasma response
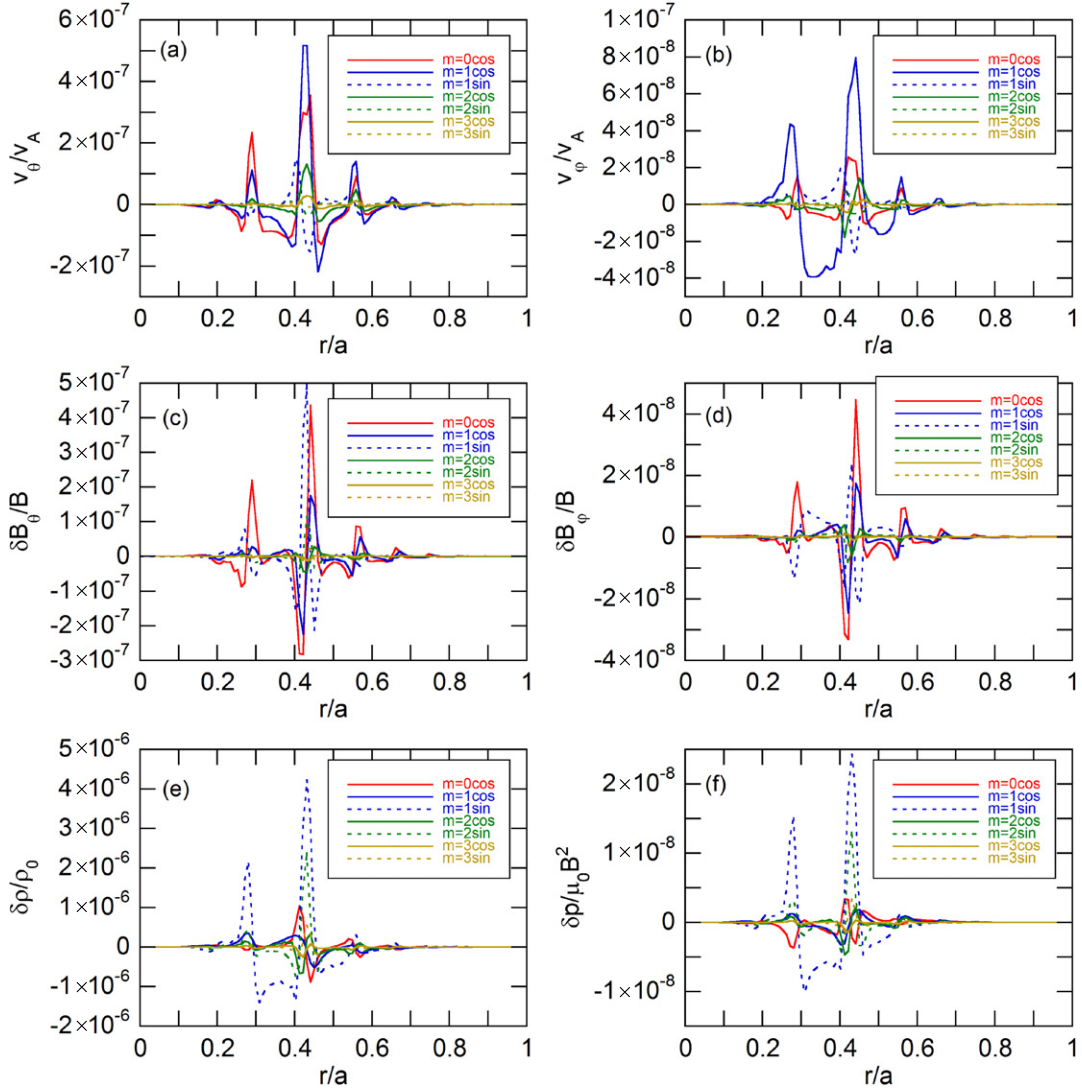
**Figure 6.** Spatial profiles of the poloidal harmonics with $n = 0$ for (*a*) poloidal flow, (*b*) toroidal flow, (*c*) poloidal magnetic field perturbation, (*d*) toroidal magnetic field perturbation, (*e*) density perturbation and (*f*) pressure perturbation during the linearly growing phase of the TAE instability at $\omega_A t = 189$. Solid and dashed curves show the $\cos(m\vartheta)$ and the $\sin(m\vartheta)$ harmonics, respectively.

$-M_{eq}(z)$ nearly cancel each other, so that the absolute value of $s - M_{eq}(z)$ is smaller than those of $s$ and $M_{eq}(z)$ by one order of magnitude. The term $2\gamma_{TAE}v_{\theta n=0}$ is shown in figure 9(*b*). We see very good agreement between the two quantities, $s - M_{eq}(z)$ and $2\gamma_{TAE}v_{\theta n=0}$. This demonstrates that the $n = 0$ fluctuations $z$ are the solution of equation (20) and the spatial profiles of the $n = 0$ fluctuations shown in figure 6 are given by $z = (2\gamma_{TAE}I + M_{eq})^{-1}(s)$ where $I$ is the unit operator. It should be emphasized that the spatial profile $z$ depends on $2\gamma_{TAE}$, the growth rate of the nonlinear source during the linear phase of the TAE instability. When the instability is saturated, the growth rate of the nonlinear source approaches zero. Then, the $n = 0$ fluctuations $z$ that are matched to the TAE linear growth are no longer a solution of equation (19) for the nonlinear phase. We found in the previous work this leads to the excitation of the geodesic acoustic mode (GAM) [20, 21]. This is different from the energetic particle driven GAM discussed in [22, 23].

We now discuss the spatial profiles of the $n = 8$ sideband. The absolute radial velocity profile is shown in figure 10. The

peak locations of each poloidal harmonic is plotted with the $n = 4$ and $n = 8$ Alfvén continua in figure 11(*a*). The $n = 8$ perturbations have twice the TAE frequency, $2\omega_{TAE}$. We see a peak of each poloidal harmonic at the $n = 8$ Alfvén continuum. This indicates that the $n = 8$ perturbations are subject to continuum damping that provides substantial dissipation even when the dissipation coefficients are reduced by 1/16 from the original case, as shown in figure 4. The continuum damping is known to be insensitive to dissipation coefficients and exist within an MHD model. It is interesting to note that the peak locations of the $n = 8$ harmonics are close to the $n = 4$ mode gap locations and relatively far from the rational surfaces of the $n = 4$ mode. We have already seen in figure 7 that the spatial profiles of the nonlinear source for the $n = 0$ poloidal flow also peak at the TAE gap locations. Thus the nonlinear coupling of the TAE mode arises primarily at the gap locations and involves predominantly two poloidal harmonics, $m$ and $m + 1$. Figure 11(*b*) is a schematic diagram for the continuum damping of the $n = 8$ sideband.
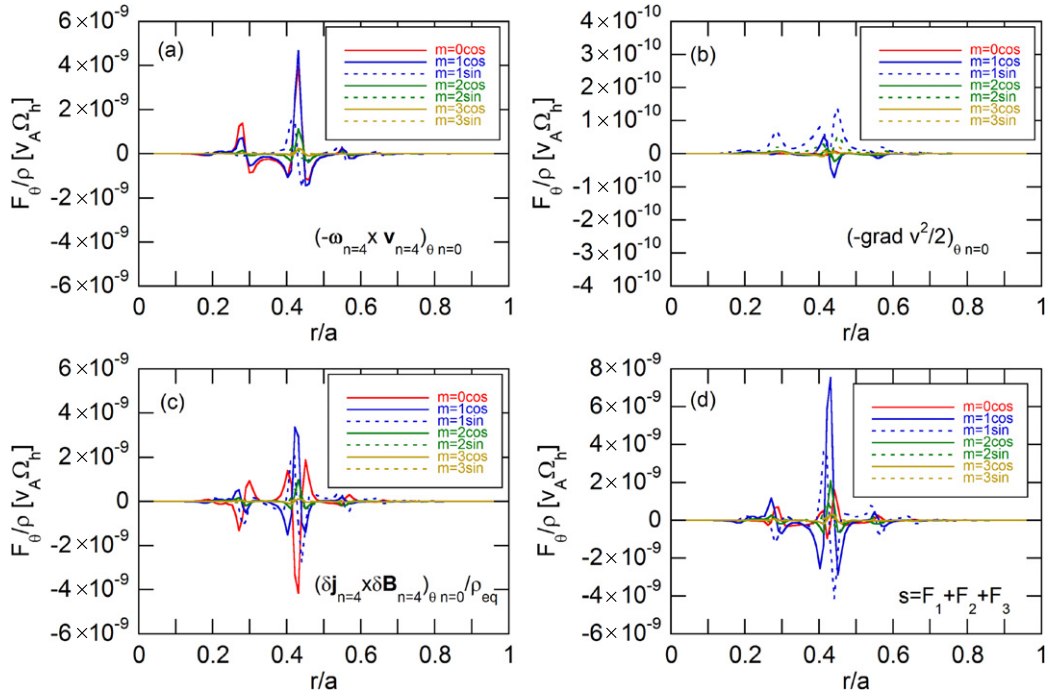
**Figure 7.** Spatial profiles of the nonlinear sources for poloidal flow with $n = 0$ at $\omega_A t = 189$; (a) $F_1$, (b) $F_2$, (c) $F_3$ and (d) $(F_1 + F_2 + F_3)$.
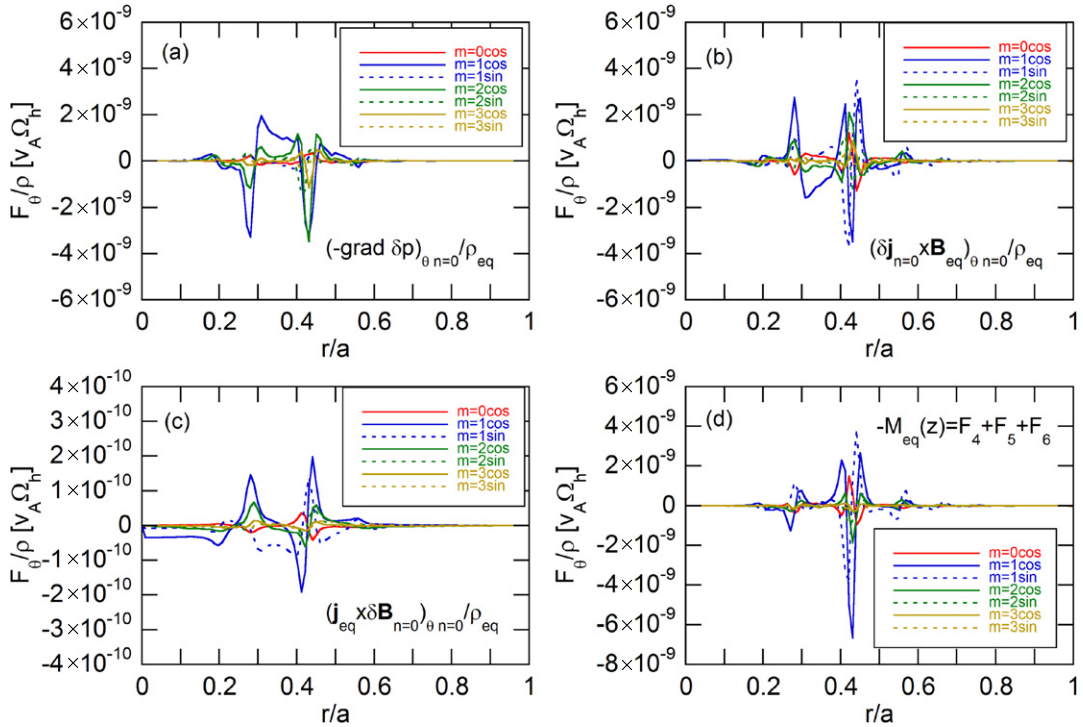


**Figure 8.** Spatial profiles of the contributions to the linear plasma response for poloidal flow with $n = 0$ at $\omega_A t = 189$; (a) $F_4$, (b) $F_5$, (c) $F_6$ and (d) $(F_4 + F_5 + F_6)$.

## 4. Summary

The nonlinear MHD effects on the evolution of the Alfvén eigenmode were investigated with hybrid simulations of an MHD fluid interacting with energetic particles. To clarify the role of the MHD nonlinearity, the nonlinear MHD results were compared with results from a reduced model, where only linear MHD equations were solved together with a nonlinear response of the energetic particles. Specifically, we studied the evolution of an $n = 4$ TAE mode destabilized by its resonant interaction with energetic particles in a tokamak plasma.

We have extended our previous simulation of the nonlinear MHD effects [1] to the regime of lower dissipation coefficients and higher numerical resolution. This step clarifies the
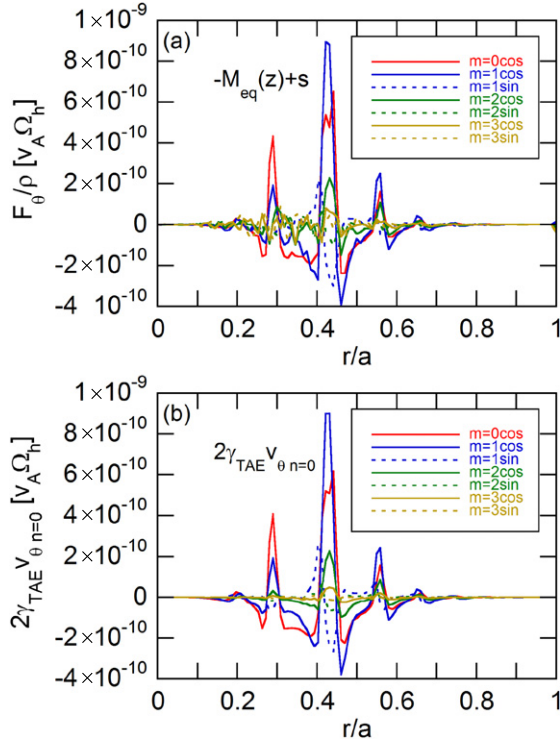
**Figure 9.** Spatial profiles of (*a*) $F_1 + F_2 + F_3 + F_4 + F_5 + F_6$ and (*b*) the $n = 0$ component of the poloidal velocity multiplied by twice the TAE growth rate at $\omega_A t = 189$.
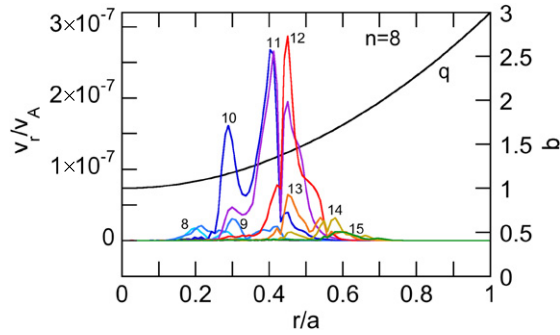


**Figure 10.** Spatial profiles of the poloidal harmonics of the absolute radial velocity with $n = 8$ during the linearly growing phase of the TAE instability at $\omega_A t = 189$. The curves are labelled by poloidal mode number $m$.

spatial profiles of the nonlinearly generated sidebands and the mechanism of sideband formation. We demonstrate that the saturation amplitude of the TAE mode is reduced due to the generation of zonal ($n = 0$) and higher-$n$ ($n \geqslant 8$) sidebands, and this reduction is attributed to the enhanced dissipation produced by the sidebands. The nonlinear sidebands that include zonal flow peak at the TAE gap locations. It is also found that the $n = 0$ poloidal flow represents a balance between the nonlinear driving force from the $n = 4$ components and the equilibrium plasma response to the $n = 0$ fluctuations. The spatial profile of the $n = 8$ sideband exhibits a resonance at the $n = 8$ Alfvén continuum. This indicates the dissipation of the $n = 8$ sideband results from the continuum damping. The higher-$n$ ($n \geqslant 8$) sidebands are essential for mode saturation in the limit of small dissipation coefficients,
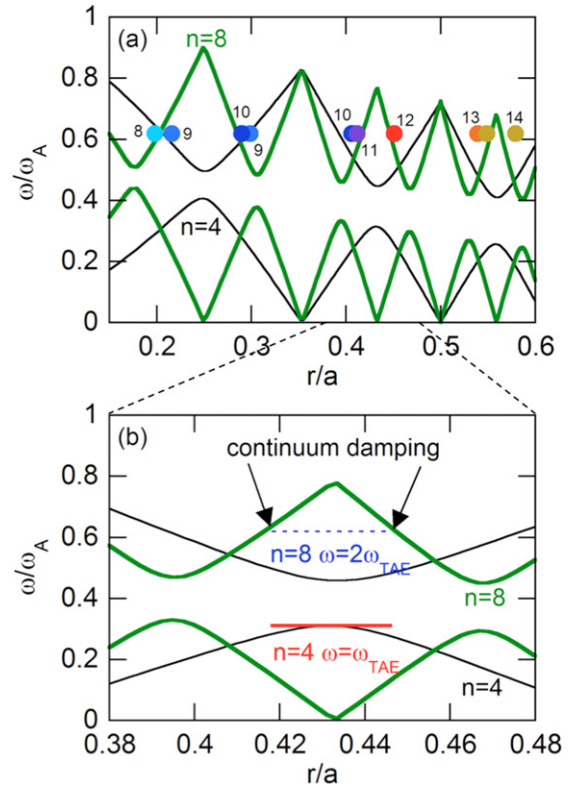


**Figure 11.** The dots (labelled by poloidal mode number $m$ in the upper panel) mark peak locations and frequencies of the poloidal harmonics of the $n = 8$ sideband. The curves show the $n = 4$ and $n = 8$ Alfvén continua. The lower panel illustrates continuum damping for the $n = 8$ sideband.

because continuum damping is independent of the dissipation coefficients.

## Acknowledgments

## References

[1] Todo Y., Berk H.L. and Breizman B.N. 2010 *Nucl. Fusion* **50** 084016
[2] Zonca F., Romanelli F., Vlad G. and Kar C. 1995 *Phys. Rev. Lett.* **74** 698
[3] Spong D.A., Carreras B.A. and Hedrick C.L. 1994 *Phys. Plasmas* **1** 1503
[4] Todo Y., Berk H.L. and Breizman B.N. 2003 *Phys. Plasmas* **10** 2888
[5] Wong K.L. *et al* 1991 *Phys. Rev. Lett.* **66** 1874
[6] Durst R.D., Fonck R.J., Wong K.L., Cheng C.Z., Fredrickson E.D. and Paul S.F. 1992 *Phys. Fluids* B **4** 3707
[7] Todo Y. and Sato T. 1998 *Phys. Plasmas* **5** 1321
[8] Todo Y., Shinohara K., Takechi M. and Ishikawa M. 2005 *Phys. Plasmas* **12** 012503
[9] Todo Y. 2006 *Phys. Plasmas* **13** 082503

[10] Todo Y., Berk H.L. and Breizman B.N. 2012 *Nucl. Fusion* **52** 033003

[11] Zonca F. and Chen L. 1992 *Phys. Rev. Lett.* **68** 592

[12] Rosenbluth M.N., Berk H.L., Van Dam J.W. and Lindberg D.M. 1992 *Phys. Rev. Lett.* **68** 596

[13] Park W. *et al* 1992 *Phys. Fluids* B **4** 2033

[14] Spong D.A., Carreras B.A. and Hedrick C.L. 1992 *Phys. Fluids* B **4** 3316

[15] Todo Y., Sato T., Watanabe K., Watanabe T.H. and Horiuchi R. 1995 *Phys. Plasmas* **2** 2711

[16] Briguglio S., Vlad G., Zonca F. and Kar C. 1995 *Phys. Plasmas* **2** 3711

[17] Wang X., Zonca F. and Chen L. 2010 *Plasma Phys. Control. Fusion* **52** 115005

[18] Littlejohn R.G. 1983 *J. Plasma Phys.* **29** 111

[19] Berk H.L., Breizman B.N. and Ye H. 1993 *Phys. Fluids* B **5** 1506

[20] Winsor N., Johnson J.L. and Dawson J.M. 1968 *Phys. Fluids* **11** 2448

[21] Hassam A.B. and Drake J.F. 1993 *Phys. Fluids* B **5** 4022

[22] Berk H.L. *et al* 2006 *Nucl. Fusion* **46** S888

[23] Fu G.Y. 2008 *Phys. Rev. Lett.* **101** 185002